Reaction Kinetics, Mechanisms and Catalysis (2019) 128:271–287
https://doi.org/10.1007/s11144-019-01616-7

Enhancement of catalytic performance over different transition metals modified CeO_2 for toluene abatement

Xuejun Zhang[1] · Jinggang Zhao[1] · Zhongxian Song[2] · Heng Zhao[1] · Wei Liu[1] · Zi'ang Ma[1] · Min Zhao[1] · Baolin Zhao[2]

Received: 1 March 2019 / Accepted: 7 June 2019 / Published online: 12 June 2019

Abstract

Pure CeO_2 and CeO_2–MO_x (M: Mn, Zr and Ni) catalysts were synthesized by the co-precipitation method and evaluated for the oxidation of toluene. The characterization showed that the specific surface area and the porous texture of catalysts were improved due to the doping of transition metal. Besides, the doping of MO_x into ceria contributed to the generation of structural defects, which could contribute to the easier storage and release of surface oxygen. Furthermore, the CeO_2–MO_x (M: Mn, Zr and Ni) catalysts exhibited higher concentration of Ce^{3+} and surface adsorbed oxygen than pure CeO_2, which could correlate with the generation of oxygen vacancies, resulting in the enhancement of redox properties. Hence, CeO_2–MnO_x exhibited the best apparent catalytic activity of toluene due to its more Ce^{3+}, structural defects and active oxygen species.

Keywords Catalytic oxidation · CeO_2–MO_x catalysts · Surface adsorbed oxygen · Redox properties

Introduction

Volatile organic compounds (VOCs) emitted from the exhaust gas emission of chemical plants and motor vehicles can easily cause environmental pollution [1–3]. Therefore, the effective removal of toluene has been urgently demanded. Researchers studied a variety of technologies to remove VOCs, such as heat incineration, biodegradation, adsorption and catalytic oxidation [4]. Among these methods, catalytic oxidation has been widely used for its superior removal efficiency of VOCs [5–7].

✉ Zhongxian Song
songzhongxian@126.com

[1] Shenyang University of Chemical Technology, Shenyang 110142, People's Republic of China

[2] Faculty of Environmental and Municipal Engineering, Henan Key Laboratory of Water Pollution Control and Rehabilitation Technology, Henan University of Urban Construction, Pingdingshan 467036, People's Republic of China

Noble metal-based catalysts exhibit the superior efficiency in catalytic performance [8]. However, its exorbitant cost, inferior stability and susceptibility to poisoning restrain its further application [9]. As substitutes, some transition metals and rare earth metals have been generally studied in catalytic oxidation of VOCs [10, 11].

Recently, the CeO_2-based materials have exhibited great potential in the catalytic oxidation of VOCs due to the excellent oxygen storage capacity (OSC) and abundant oxygen vacancies. Specifically, the reversible Ce^{4+}/Ce^{3+} redox cycles promote the mobility of reactive oxygen species. Ce-M-O_x (M is the transition metal) mixed oxide material catalyst exhibits superior VOCs oxidation performance compared to the corresponding single metal oxide catalyst [12–15]. Venkataswamy et al. [16] claimed that $Ce_{0.7}Mn_{0.3}O_{2-\delta}$ catalysts presented more surface oxygen defects or hydroxyl-like groups than pure CeO_2, which could contribute to the improvement of catalytic activity. Li et al. [17] revealed that the roles of adsorption oxygen and lattice oxygen species over $CuO/Ce_{0.7}Mn_{0.3}$ were ambiguous in the catalytic removal of benzene. It was reported that the doping of ZrO_x could enhance the thermal stability of catalyst due to higher binding energy of Zr and O [18, 19]. Hu et al. [20] proved that the introduction of NiO_x could optimize the reducibility for the total oxidation of propane. In spite of this, it was still not clear which transition metal could better improve the catalytic oxidation capacity of the catalyst. We found that the addition of different transition metals can promote the catalytic performance of Ce-based catalysts in VOCs oxidation. However, different metals exhibited different effects on their oxidation properties and chemical valence states. It is still necessary to discuss the effect of metal doping on CeO_2 catalysts in a specific catalyst environment. Therefore, we selected several common metals to modify the performance of the catalyst, in order to further develop and enrich the theory of catalytic oxidation of VOCs.

In this work, the CeO_2 and CeO_2–MO_x (M: Mn, Zr and Ni) catalysts were synthesized by co-precipitation method. In order to investigate the influence of different transition metals on the catalytic performance of CeO_2, the CeO_2–MO_x (M: Mn, Zr and Ni) catalysts have been characterized by powder X-ray diffraction patterns (XRD), N_2 adsorption–desorption, X-ray photoelectron spectroscopy (XPS), Raman spectra, H_2 temperature-programed reduction (H_2-TPR) and oxygen temperature-programmed desorption (O_2-TPD) techniques.

Experimental

Chemicals and materials

All the reagents involved in catalyst synthesis were A.R. grade and were used directly. Concentrated $NH_3{\cdot}H_2O$ solution, cerium(III) nitrate hexahydrate ($Ce(NO_3)_3{\cdot}6H_2O$), manganese(II) nitrate ($Mn(NO_3)_2$), nickel(II) nitrate hexahydrate ($Ni(NO_3)_2{\cdot}6H_2O$), zirconium(IV) nitrate pentahydrate ($Zr(NO_3)_4{\cdot}5H_2O$) and toluene were supplied from Sinopharm Chemical Reagent Co., Ltd. (Shenyang, China).

Catalyst preparation

The procedures for synthesis of CeO_2–MO_x (M: Mn, Zr and Ni) by co-precipitation were as follows: the desired amount of M nitrates was dissolved in 100 mL of deionized water in beakers under stirring condition. After complete dissolution, the corresponding amount of $Ce(NO_3)_3{\cdot}6H_2O$ was dissolved into the above solution to obtain the mixed solution ($MO_x/CeO_2 = 25$ wt%). The ammonia solution was added drop by drop to the aforementioned mixed solution with vigorous stirring, until the pH value reached 10. Then the beakers containing the precipitate were transferred to the heat-collecting thermostatic magnetic stirrer and stirred at 80 °C for 4 h. After resting 12 h at room temperature, the precursor precipitate was screened out from the supernatant by the suction filter device and washed several times with distilled water until the pH reached 7. The obtained solid precursor was dried at 100 °C for 12 h and then calcined in a muffle furnace at 550 °C for 5 h in air (the heating rate of 3 °C min^{-1}). The obtained catalysts were denoted as CeO_2–MnO_x, CeO_2-ZrO_x and CeO_2–NiO_x. For comparison purpose, pure CeO_2 sample was also prepared under similar conditions using cerium nitrate as the precursor and represented as CeO_2.

Measurement of catalytic activity

The catalytic combustion of toluene was performed on the fixed bed reactor (i.d. = 8.0 mm) to measure catalytic performance using 0.1 mL of catalysts (40 − 60 mesh), in the temperature range 200–360 °C. The simulated gas atmosphere was 500 ppm of toluene diluted in 20 V % O_2/N_2 mixture (100 mL/min) resulting in gas hour space velocity (GHSV) of 60,000 h^{-1}. In order to stabilize the system, the gaseous mixture was introduced over the catalyst at room temperature before heating and the on-line gas chromatography (GC, FULI 9790 II) equipped with FID detectors was adopted to analyze the composition of the outlet gas.

The following formulas were used to calculate the conversion of toluene (C_t) and CO_2 generation rate $\left(C_{CO_2}\right)$:

The conversion of toluene (C_t):

$$C_t(\%) = \frac{(toluene)_{in} - (toluene)_{out}}{(toluene)_{in}} \times 100$$

where $(toluene)_{in}$ and $(toluene)_{out}$ denotes the inlet and outlet concentrations of toluene.

The CO_2 generation rate $\left(C_{CO_2}\right)$:

$$C_{co_2}(\%) = \frac{(Cco_2)_{out}}{7 \times (toluene)_{in}} \times 100$$

where $\left(C_{CO_2}\right)_{out}$ was the CO_2 outlet concentration.

Catalyst characterization

Textural properties of the samples were derived by nitrogen adsorption–desorption at − 196 °C using an analyzer of SSA-6000 from Beijing Builder Electronic Technology Company. Before the measurement, the catalysts were degassed at 250 °C for 3 h. The specific surface area (S_{BET}) and porous volume of each catalyst were determined using the Brunauer–Emmett–Teller (BET) and the Barrett-Joyner-Halenda (BJH) methods.

Powder X-ray diffraction (XRD) patterns of all samples were collected on Brucker diffractometer (D8 Advance) and it adopted Cu K_α radiation at the 2θ range 10–80° with a scanning step size of 0.02° and scanning speed of 1.5 s.

Raman spectra were operated on a Raman microscope (Renishaw-2000) at a resolution of 2 cm^{-1} plus with an argon ion laser of 514.5 nm wavelength as exciting source.

Chemical state of surface elements was recorded by an ESCALAB 250 X-ray photoelectron spectroscopy (XPS) with Al K_α X-ray radiation for the X-ray source (Thermo Fisher Scientific, USA). C1 s core excitation at 284.6 eV was adopted to calibrate the electron binding energy (BE) scale. The operation process was as follows: First, the sample sheet was pasted on the conductive adhesive of the sample tray; the tray was then vacuumed in a preparation chamber for 12 h (The instrument was filled with nitrogen before operation); finally, the sample in the preparation chamber was moved in situ to the analysis chamber (vacuum state) for scanning. No high temperature treatment during the whole process. Peak fitting was processed with XPSPEAK. The fitting procedure was allowed determining the peak position, height and width.

The temperature programmed reduction of hydrogen (H_2-TPR) was conducted on a chemisorption analyzer PCA-1200 (Beijing Builder Electronic Technology Company) with a quartz U-shaped tubular reactor. A 20 mg of each catalyst was packed into the reactor and operated with 30 mL/min of high purity nitrogen at 400 °C for 40 min to purify the sample, and then cooled to 100 °C. The temperature was increased to 900 °C (10 °C/min) with gas flowing of 5 V % H_2/Ar (30 mL/min).

On the same chemisorption analyzer, the experiments of oxygen temperature programmed desorption (O_2-TPD) detected the oxygen mobility of catalysts. 200 mg samples were degassed with helium (30 mL/min) at 200 °C for 1 h in the quartz microreactor. After cooling down to 50 °C, 20 V % O_2/He of 30 mL/min mixture gas was introduced for 1 h. Subsequently, the catalysts were heated at a rate of 10 °C min^{-1} from 50 to 900 °C in a helium atmosphere.

Results and discussion

Evaluation of catalytic oxidation

The catalytic oxidation performances of the samples in the toluene catalytic combustion are displayed in Fig. 1. As shown in Fig. 1a, all the catalysts exhibited an upward trend as the reaction temperature increased. Pure CeO_2 exhibited the T_{90}

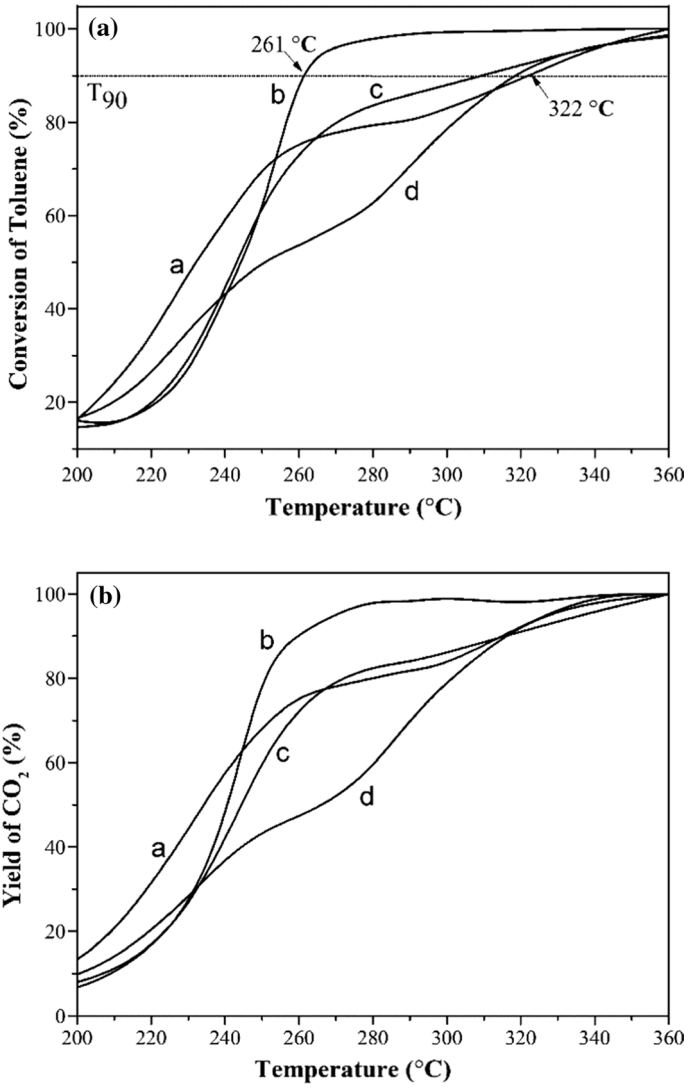

Fig. 1 Catalytic performances for toluene destruction over **a** CeO_2, **b** CeO_2–MnO_x, **c** CeO_2-ZrO_x and **d** CeO_2–NiO_x catalysts. Reaction conditions: catalysts volume = 0.1 mL, toluene concentration = 500 ppm, GHSV = 60,000 h^{-1}: (**a**) conversion of toluene and (**b**) yield of CO_2

(the temperature at which the C_t reached 90%) value at 322 °C. After doping transition metal oxide, the sequence of T_{90} over the samples was as follows: CeO_2–MnO_x (261 °C) < CeO_2–ZrO_x (309 °C) < CeO_2–NiO_x (316 °C). Hence, the catalytic activity for toluene over CeO_2-based catalysts was improved after the addition of transition metal, especially for CeO_2–MnO_x catalyst. Moreover, the CeO_2 catalysts displayed unsatisfactory CO_2 selectivity at high temperature in comparison with CeO_2–MO_x (M: Mn, Zr and Ni), especially for CeO_2–MnO_x, suggesting that the doping of

transition metal oxide could improve the CO_2 selectivity at high temperatures. In brief, CeO_2–MnO_x exhibited the best CO_2 selectivity and catalytic performance of toluene, and the value of CO_2 yield could reach 100% at 280 °C and above 90% toluene conversion was obtained at 261 °C.

N_2 adsorption–desorption

The N_2 adsorption–desorption isotherms of CeO_2 and CeO_2–MO_x (M: Mn, Zr and Ni) catalysts with the BJH pore-size distributions are presented in Fig. 2a, b. As shown in Fig. 2a, all samples displayed the typical type IV isotherms with H3-type

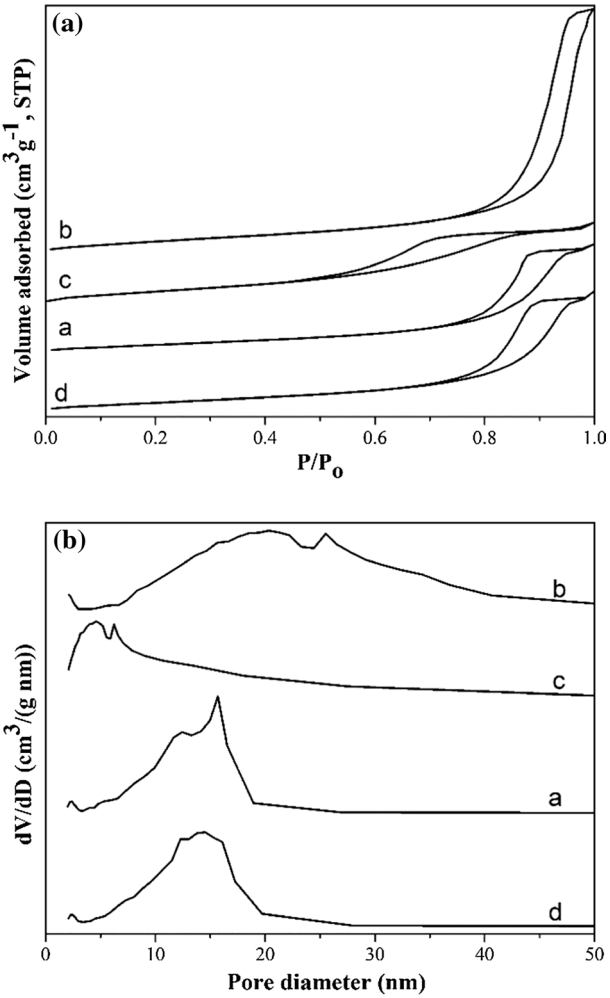

Fig. 2 (**a**) N_2 adsorption–desorption isotherms and (**b**) pore-size distributions of the four catalysts (**a** CeO_2, **b** CeO_2–MnO_x, **c** CeO_2–ZrO_x and **d** CeO_2–NiO_x)

hysteresis loops, which indicated the existence of mesoporous structure [5, 21]. Furthermore, the hysteresis loop of CeO_2 could be observed at the P/P_0 value of 0.8. Compared to CeO_2, the hysteresis loop of CeO_2–MO_x shifted to lower values, which was representative of more mesopores in the samples [18, 22]. It was reported that the higher S_{BET} and pore volume were believed to weaken transfer resistance and optimize the adsorption capacity of VOCs [19]. Thereby, the CeO_2–MnO_x catalyst showed the excellent catalytic performance compared with CeO_2. Fig. 2b shows the pore-size distributions of all samples. Obviously, each sample shows the distribution range from 5 to 50 nm, which was the feature of typical mesoporous material. The textural properties of the prepared catalysts are summarized in Table 1. The S_{BET} of CeO_2–MO_x was larger than that of CeO_2 (49 m^2g^{-1}). CeO_2- ZrO_x exhibited the largest S_{BET} (72 m^2g^{-1}), followed by CeO_2–MnO_x with the S_{BET} of 63 m^2g^{-1}, and the CeO_2–NiO_x catalyst possessed the S_{BET} of 50 m^2g^{-1}. Obviously, the structural and surface properties of the prepared catalysts were directly optimized by the type of doped metals, which was benefited to the removal activity of toluene at high temperatures.

XRD patterns

Fig. 3 presents the XRD patterns of CeO_2 and CeO_2–MO_x (M: Mn, Zr and Ni) samples. From Fig. 3a, the feature diffraction peaks of cubic CeO_2 (PDF# 43-1002) were detected on the samples, and no other diffraction peaks were observed, indicating that the added M species existed the high dispersed state or amorphous metal species [17, 20, 23, 24]. Additionally, the diffraction peaks of CeO_2–MO_x were slightly shifted to high angle side (shown in Fig. 3b) compared to pure CeO_2 due to the incorporation of M ions into the ceria lattice, resulting in the formation of Ce-M solid solution, which contributed to improving the oxygen storage/release capacity [16, 25, 26]. Previous studies reported that the amorphous structure of the metal oxide catalysts or the homogeneous distribution of surface metal oxides might be a reason for superior catalytic activity of VOCs oxidation [27–29]. As revealed in Fig. 2, the CeO_2–MO_x oxides showed superior catalytic activity and CO_2 selectivity than CeO_2, which was attributed to the formation of Ce-MO_x solid solution, high distribution of metal oxides or amorphous structure of the metal oxides.

Table 1 BET surface area, pore volume and Raman results of CeO_2 and CeO_2–MO_x (M: Mn, Zr and Ni) catalysts

Catalysts	S_{BET} (m^2g^{-1})	Pore volume (cm^3g^{-1})	C^a_{ov} (%)
CeO_2	49	0.169	7.4
CeO_2-ZrO_x	72	0.131	11.6
CeO_2–MnO_x	63	0.368	15.5
CeO_2–NiO_x	50	0.184	12.1

[a]The relative concentration of oxygen vacancies (C_{ov}) was calculated by the equation: $C_{ov}=A_{600}/A_{462}$. Where A_x was the Raman peak areas at the position of x cm^{-1}

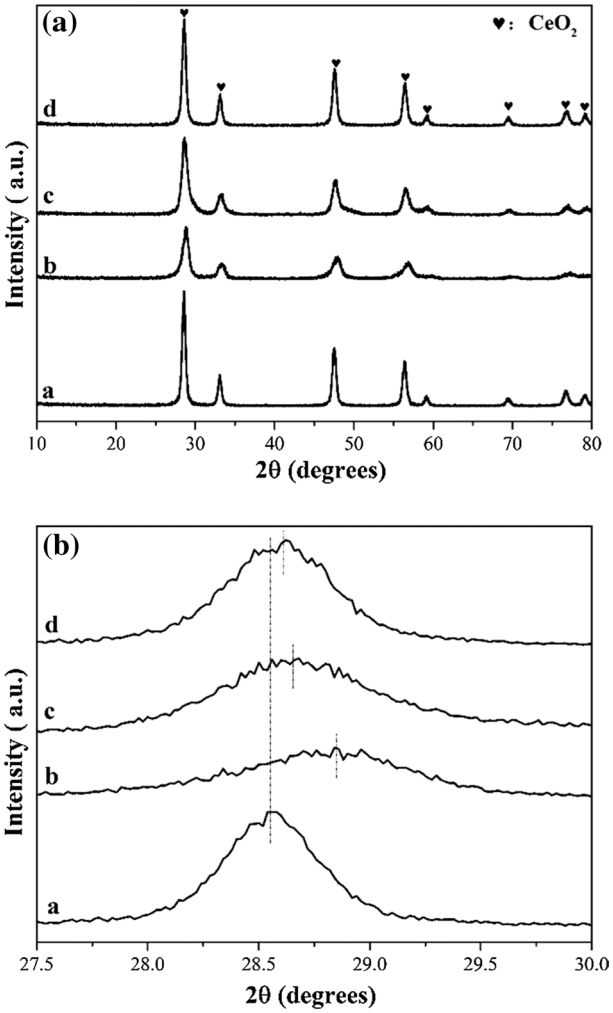

Fig. 3 XRD patterns of **a** CeO_2, **b** CeO_2–MnO_x, **c** CeO_2–ZrO_x and **d** CeO_2–NiO_x catalysts: (**a**) 2θ:10–80° and (**b**) 2θ: 27.5–30°

Raman studies

Raman spectroscopy was conducted to obtain more structural information for the CeO_2 and CeO_2–MO_x (M: Mn, Zr and Ni) catalysts, and the results are displayed in Fig. 4. The sharp bands centered at about 462 cm^{-1} were assigned to the symmetric stretching vibrations (F_{2g}) of cubic fluorite ceria [30, 31]. Another weak peak at about 600 cm^{-1} in CeO_2–MO_x samples was attributed to the presence of oxygen vacancies, which was proposed to promote the redox reaction of the catalysts [30]. In addition, the characteristic vibrational modes of MnO_2 were detected in CeO_2–MnO_x catalyst at 640 cm^{-1} [32]. For CeO_2-ZrO_x and CeO_2–NiO_x catalysts,

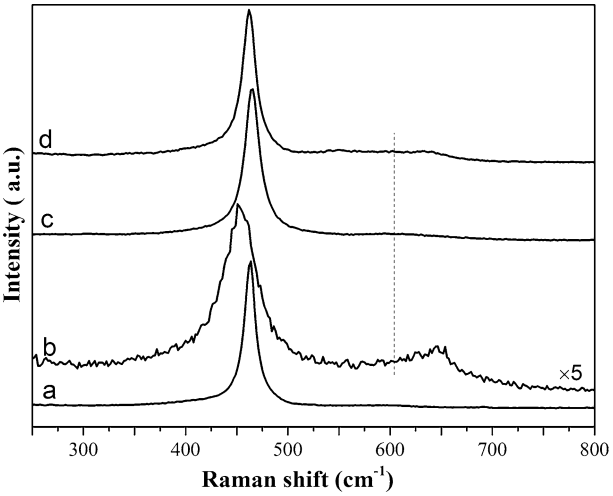

Fig. 4 Raman spectra of **a** CeO_2, **b** CeO_2–MnO_x, **c** CeO_2–ZrO_x and **d** CeO_2–NiO_x materials

no Raman peaks attributed to Zr and Ni metal oxides could be observed in these two samples, respectively, which could be attributed to a relatively homogeneous dispersion of Zr and Ni metal oxides on CeO_2 or the incorporation into the lattice of CeO_2 [30]. It was worth noting that the deformation and shift of position for ceria F_{2g} bands were produced in the CeO_2–MO_x catalysts, confirming the incorporation of M (M: Mn, Zr and Ni) metal ions into the CeO_2 lattice structure [33]. Especially in the case of the CeO_2–MnO_x sample, the width of ceria F_{2g} bands was widened in a strong way, and its position shifted toward 453 cm^{-1}, which contributed to the introduction of Mn ions into CeO_2 [32, 34]. It was reported that the doping of other cations into ceria lattice contributed to the generation of structural defects, which could correlate with the creation of oxygen vacancies and favor oxygen mobility [26, 35]. Thus, the relative concentration of oxygen vacancies (C_{ov}) was calculated using the ratios of the peak areas of the Raman spectra and the results are summarized in Table 1. Obviously, CeO_2–MO_x showed higher C_{ov} than that of pure CeO_2. The order of the C_{ov} was: $CeMnO_x$ (15.5%) > $CeNiO_x$ (12.1%) > $CeZrO_x$ (11.6%) > CeO_2. (7.4%), which was basically consistent with toluene catalytic oxidation activity results, confirming that the oxygen vacancies were crucial sites in the reaction. The CeO_2–MO_x catalysts exhibited a distinctly higher C_{ov} than pure CeO_2, indicating that the transition metal oxides were successfully introduce and thereby the C_{ov} of the Ce-based catalysts increased. Hence, the CeO_2–MnO_x exhibited superior performance of catalytic removal toluene than pure CeO_2.

XPS studies

In order to investigate the surface oxidation states of CeO_2 and CeO_2–MO_x (M: Mn, Zr and Ni) catalysts, Fig. 5 shows the XPS spectra of Ce 3d and O 1 s. According to the previous publications, the six peaks labeled as U, U″, U‴, V, V″ and V‴

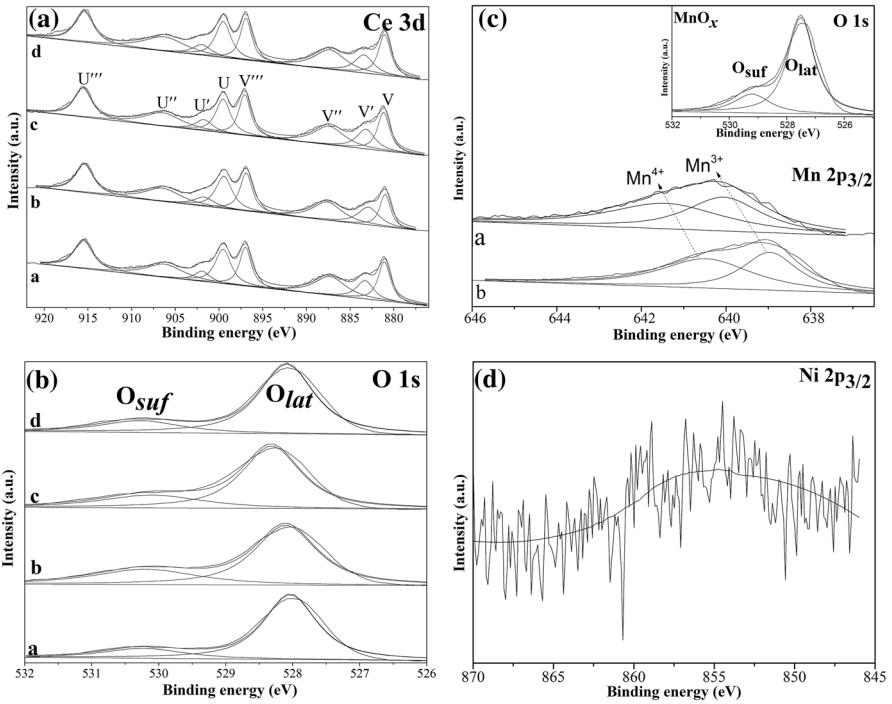

Fig. 5 XPS patterns of Ce 3d (**a**) for **a** CeO_2, **b** CeO_2–MnO_x, **c** CeO_2–ZrO_x and **d** CeO_2–NiO_x catalysts; O 1 s (**b**) for **a** CeO_2, **b** CeO_2–MnO_x, **c** CeO_2–ZrO_x, **d** CeO_2–NiO_x and pure MnO_x (inset in (**c**)) catalysts; Mn $2p_{3/2}$ (**c**) for **a** CeO_2–MnO_x and **b** pure MnO_x; Ni $2p_{3/2}$ (**d**) for CeO_2–NiO_x catalyst

in Fig. 5a are connected to Ce^{4+} ions, while the other two peaks U′ and V′ were attributed to the Ce^{3+} ions [34–36]. It was remarkable that the BE of Ce 3d over CeO_2–MnO_x catalyst presented a tendency of decline compared with pure CeO_2. It might be due to the interaction between manganese and cerium oxides, which affected the electron state of cerium, resulting in an improvement of catalytic oxidation ability and the superior catalytic performance. The surface relative concentrations of Ce^{3+} ions ($Ce^{3+}/(Ce^{3+}+Ce^{4+})$) for the samples were quantitatively analyzed and the results are summarized in Table 2. The $Ce^{3+}/(Ce^{3+}+Ce^{4+})$ ratio decreased in

Table 2 XPS results of CeO_2, CeO_2–MO_x (M: Mn, Zr and Ni) and pure MnO_x catalysts

Catalysts	$Ce^{3+}/(Ce^{4+}+Ce^{3+})$ (%)	$O_{suf}/(O_{lat}+O_{suf})$ (%)	$Mn^{3+}/(Mn^{4+}+Mn^{3+})$ (%)
CeO_2	13.1	19.1	–
CeO_2–MnO_x	16.2	30.3	46.6
CeO_2-ZrO_x	15.3	26.2	–
CeO_2–NiO_x	14.1	20.2	–
MnO_x	–	20.6	43.7

the order of CeO_2–MnO_x (16.2%)>CeO_2-ZrO_x (15.3%)>CeO_2–NiO_x (14.1%)>CeO_2 (13.1%). It was obvious that the relative concentration of Ce^{3+} ions of CeO_2–MnO_x catalyst was the largest among the samples. It was reported [21, 35] that a higher Ce^{3+} content promoted the formation of the charge imbalance, oxygen vacancies and unsaturated chemical bonds on the surface of catalysts, which could improve the catalytic oxidation property of toluene. Besides, the mobility of the active oxygen species was improved by more amounts of Ce^{3+}, which could enhance the catalytic performance for VOCs oxidation. Thereby, the CeO_2–MnO_x catalyst showed the excellent catalytic activity.

Fig. 5b shows that the XPS spectra of O 1 s for all catalysts, which was divided into two peaks. One peak at lower BE was assigned to the lattice oxygen (O_{lat}), and the other peak at higher BE corresponded to surface oxygen (O_{suf}) including oxygen defect or adsorbed oxygen [34, 37]. Obviously, the binding energy of all peaks (O_{lat} and O_{suf}) in CeO_2–MO_x shifted to higher value compared with pure CeO_2, which indicated that the interaction between CeO_2 and MO_x (M: Mn, Zr and Ni) existed. In order to investigate the influence of various oxygen species, the ratios of $O_{suf}/(O_{lat}+O_{suf})$ were calculated by integrating O 1 s spectra peak areas and the values are summarized in Table 2. The O_{suf} concentration of other catalysts followed by the sequence: CeO_2–MnO_x (30.3%)>CeO_2-ZrO_x (26.2%)>CeO_2–NiO_x (20.2%)>CeO_2 (19.1%). The similar trend was observed in the relative concentration of Ce^{3+} ions. In addition, as previously reported in the literature [35, 38], the higher amounts of surface Ce^{3+} were probably related to abundant surface oxygen defects, which was helpful for an increase in surface adsorbed oxygen, highlighting the importance of the amount of adsorbed oxygen and oxygen defects on the catalytic activity of samples. It was reported that surface adsorbed oxygen species were vital for most of the catalytic oxidation reactions due to the greater mobility than lattice oxygen [35, 38]. Hence, the CeO_2–MnO_x catalyst with the highest $O_{suf}/(O_{lat}+O_{suf})$ showed the best toluene conversion.

Additionally, Fig. 5c shows the Mn $2p_{3/2}$ XPS spectra of pure MnO_x and CeO_2–MnO_x catalysts, which were further resolved into two components. The peaks at low BE were attributed to the Mn^{3+} and the high BE peaks were assigned to Mn^{4+}, which indicated the coexistence of Mn^{3+} and Mn^{4+} on the surface of catalysts [21, 39]. Consistent with recent reports, the BE of Mn $2p_{3/2}$ peak in CeO_2–MnO_x shifted to higher value compared with pure MnO_x, which indicated that the interaction between CeO_2 and MnO_x and it affected the oxidation state of manganese species [40]. In addition, the surface ion ($Mn^{3+}/(Mn^{4+}+Mn^{3+})$) ratios and $O_{suf}/(O_{lat}+O_{suf})$ calculated by integrating spectra peak areas are summarized in Table 2. Obviously, the CeO_2–MnO_x catalyst showed the higher $Mn^{3+}/(Mn^{4+}+Mn^{3+})$ ratio (46.6%) than that of pure MnO_x (43.7%) and the $O_{suf}/(O_{lat}+O_{suf})$ showed the same trend. Mn^{3+} was easier to lose the oxygen species than that on Mn^{4+} at low-temperature due to its weak binding capacity to oxygen [41]. Furthermore, it was reported that the presence of more Mn^{3+} contributed to the formation of oxygen vacancies and structural defects, which could enhance the redox properties of the catalyst during the reaction processes [42].

The Ni 2p XPS analysis of CeO_2–NiO_x catalyst is shown in Fig. 5d. Obviously, a broad peak appearing at about 855 eV was corresponded to Ni $2p_{3/2}$ and it confirmed

the presence of Ni species [35]. Previous studies reported that the Ni $2p_{3/2}$ peaks from 850.0 to 857.0 eV could be divided into metallic nickel (Ni^0) and nickel oxide (Ni^{2+}) at 852.5 and 855.5 eV, while peaks from 857.0 to 865.0 eV were attributed to satellite peaks [43, 44]. The coexisted of two nickel species on the surface of catalyst contributed to electron transfer and promoted the redox capacity of the catalyst. Unfortunately, it was difficult to distinguish the nickel oxide state due to the weak signal resulting from the uniform dispersion of low nickel content in the bulk catalyst.

H_2-TPR

In order to investigate the reducibility of each catalyst, H_2-TPR analyses were carried out and the profiles are shown in Fig. 6a. What is more, the corresponding hydrogen consumption of each reduction region is summarized in Table 3. As depicted in Fig. 6a, CeO_2 exhibited two reduction peaks centered at around 510 and 760 °C, which were assigned to the reduction of surface CeO_2 and bulk CeO_2, respectively [30, 45]. For CeO_2–NiO_x sample, it presented two main reduction peaks with the maxima at 320 and 770 °C, respectively. The latter might be related to the reduction of bulk CeO_2, and the former was assigned to the reduction of NiO species and partial ceria [46]. Compared to the pure CeO_2 catalyst, the reduction of the former peak was initiated at lower temperatures (< 200 °C) and the intensity was stronger, which indicated a significant improvement in reducibility due to the interaction between NiO and CeO_2. As to CeO_2-ZrO_x sample, it exhibited two reduction features centered at about 550 and 750 °C, which could be assigned to the reduction of surface and bulk CeO_2 [45, 47, 48]. Interestingly, compared to CeO_2, the peak intensity of CeO_2-ZrO_x was enhanced and the range was broadened, which was attributed to the higher mobility of lattice oxygen due to the formation of vacancies or structural defects, further promoting the redox property and then improving catalytic performance [48, 49]. For CeO_2–MnO_x, the peak at 220 °C was related to the reduction of Mn^{4+} to Mn^{3+}. The peak at about 320 °C was assigned to the reduction of Mn^{3+} to Mn^{2+} together with the possible reduction of surface ceria. The peak at 730 °C was the reduction peak of bulk CeO_2 [15, 50]. Particularly, the locations of the three reduction peaks shifted to lower temperature and the intensity was greatly enhanced compared to CeO_2. These phenomena indicated that the interaction between CeO_2 and MnO_x improved the redox property and contributed to the improvement of the catalytic oxidation of the toluene. In addition, the better low-temperature reducibility of CeO_2–MnO_x confirmed by the hydrogen consumption is summarized in Table 3. Obviously, CeO_2–MO_x exhibited larger amounts of low temperature (< 620 °C) and the H_2 consumption as follows: CeO_2 (190.7) < CeO_2–NiO_x (293.9) < CeO_2-ZrO_x (539.2) < CeO_2–MnO_x (1871.6). Obviously, the low reducibility of catalysts were improved variously. In addition, the total H_2 consumption of the catalysts showed the same trend as the hydrogen consumption at low temperature: CeO_2 (1009.8) < CeO_2–NiO_x (1013.4) < CeO_2-ZrO_x (1088.3) < CeO_2–MnO_x (2200.6), which implied that the reducibility of catalyst was improved variously due to the introduction of Mn, Zr and Ni element into CeO_2.

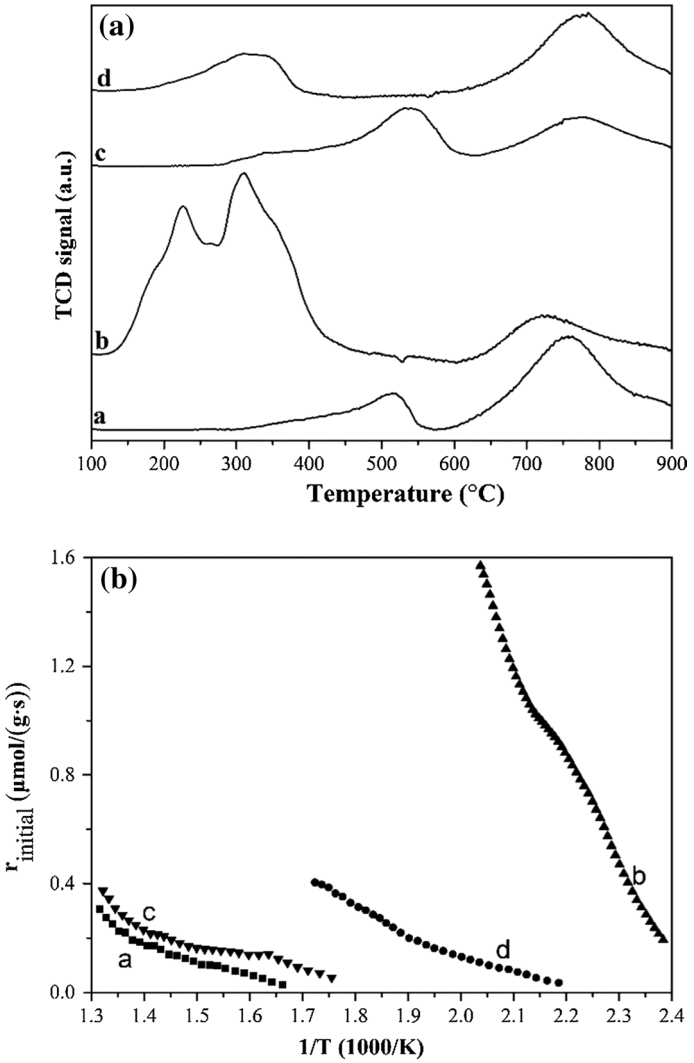

Fig. 6 (**a**) H_2 -TPR profiles and (**b**) initial H_2 consumption rate ($r_{initial}$) at low temperature for **a** CeO_2, **b** CeO_2–MnO_x, **c** CeO_2–ZrO_x and **d** CeO_2–NiO_x catalysts

In order to study the catalytic performance deeply, the differences of reducibility for all catalysts were estimated by the initial H_2 consumption rate ($r_{initial}$) and the profiles are shown in Fig. 6b. The order of low temperature reducibility was as follows: $CeO_2 < CeO_2$–$ZrO_x < CeO_2$–$NiO_x < CeO_2$–MnO_x. The H_2-TPR results indicated that the incorporation of M metal cations into the CeO_2 crystallites could promote the reducibility of the catalyst, which might attribute to the appearance of abundant reducible oxygen species.

Table 3 The results of H_2-TPR and O_2-TPD

Catalysts	T_H^a	X_H^b	$\sum X_H^c$	T_O^a	X_O^b	$\sum X_O^c$
CeO_2	309–555	190.7	1009.8	141–771	10.7	10.7
	558–900	819.1				
CeO_2–MnO_x	122–600	1871.6	2200.6	107–560	40.3	40.5
	620–900	329.0		802–848	0.2	
CeO_2–ZrO_x	264–620	539.2	1088.3	200–581	17.0	17.0
	628–900	549.1				
CeO_2–NiO_x	147–388	293.9	1013.4	332–625	11.0	18.4
	620–900	719.5		630–850	7.0	

[a]The temperature interval of H_2-TPR peak (T_H, °C) and O_2-TPD peak (T_o, °C)

[b]The H_2 consumption (X_H, umol/g) and the amount of desorbed oxygen (X_O, umol/g)

[c]The total H_2 consumption ($\sum X_H$, umol/g) and the total amount of desorbed oxygen ($\sum X_O$, umol/g)

O_2-TPD experiment

The O_2-TPD was used to investigate the mobility of oxygen species in all catalysts, and the results are shown in Fig. 7. All the samples displayed desorption peaks at low temperature (< 500 °C), which could be assigned to the desorption of physisorbed oxygen and chemisorbed oxygen from the surface of materials. Besides, the peak at high temperature (> 500 °C) was ascribed to lattice oxygen (O_{lat}) [10, 37]. Compared with pure CeO_2 catalyst, the surface adsorbed oxygen of CeO_2–ZrO_x

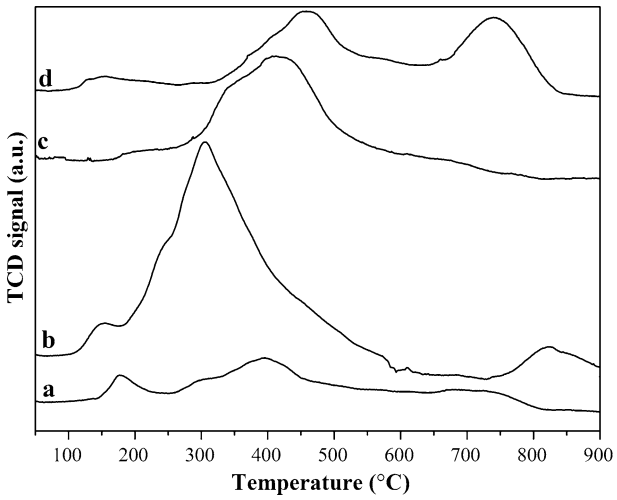

Fig. 7 O_2-TPD profiles at the temperature range of 50–900 °C for **a** CeO_2, **b** CeO_2–MnO_x, **c** CeO_2–ZrO_x and **d** CeO_2–NiO_x catalysts

catalyst shifted to higher temperatures and the intensity was enhanced. The phenomena indicated that the addition of ZrO_x into CeO_2 could improve the thermal stability, and then increased the contents of surface oxygen significantly [51]. For the CeO_2–NiO_x catalyst, the intensities of surface adsorbed oxygen and lattice oxygen were much higher than that of CeO_2, which was favorable for high catalytic activity for VOCs combustion [52]. As for CeO_2–MnO_x catalyst, the surface adsorbed oxygen moved to lower temperature. It was proved that the oxygen species got easier to be released from the surface of CeO_2–MnO_x catalyst. The desorption of lattice oxygen for CeO_2–MnO_x deviated to 822 °C, which could be attributed to the interaction between CeO_2 and MnO_x. In addition, the intensities of desorption peaks of CeO_2–MnO_x catalyst were obviously stronger than that of pure CeO_2, especially the surface adsorbed oxygen [37]. In addition, based on the accurate quantitative analysis of the profiles, the amount of desorbed oxygen in each peak and total desorbed oxygen is listed in Table 3. Obviously, CeO_2–MO_x showed larger desorbed amounts of surface oxygen and total oxygen and the order total desorbed oxygen was as follows: CeO_2 (10.7) < CeO_2–ZrO_x (17.0) < CeO_2–NiO_x (18.4) < CeO_2–MnO_x (40.7), which indicated that CeO_2–MO_x exhibited the higher capacity for adsorbed oxygen. The phenomena indicated that more surface adsorbed oxygen species formed and the mobility was improved tremendously by introduction of MO_x.

Conclusions

The physicochemical properties of the CeO_2 and CeO_2–MO_x (M: Mn, Zr and Ni) materials were characterized by N_2 adsorption–desorption, XRD, Raman, XPS, H_2-TPR and O_2-TPD characterization techniques. The results showed that CeO_2–MO_x catalysts were mainly mesoporous structures and the transition metal ions were introduced into the fluorite lattice, which contributed to the interaction between CeO_2 and MO_x. CeO_2–MO_x catalysts showed the better catalytic combustion ability of toluene and CO_2 selectivity than CeO_2.The T_{90} of toluene combustion was as follows: CeO_2–MnO_x (261 °C) < CeO_2–ZrO_x (310 °C) < CeO_2–NiO_x (316 °C) < CeO_2 (322 °C). CeO_2–MnO_x catalyst exhibited the more concentration of Ce^{3+}, surface adsorbed oxygen, structural defects and the optimal redox properties, and CeO_2–MnO_x catalyst showed the highest catalytic efficiency.

Acknowledgements This work is supported by the National Natural Science Foundation of China (No. 21872096) and Doctoral Research Start-up Project of Henan University of Urban Construction (No. 990/Q2017011).

References

1. Zhang C, Guo Y, Guo Y, Lu G, Boreave A, Retailleau L, Baylet L, Giroir-Fendler A (2014) Appl. Catal. B: Environ. 148–149:490–498
2. Sihaib Z, Puleo F, Garcia-Vargas J, Retailleau L, Descorme C, Liotta L, Valverde J, Gil S, Giroir-Fendler A (2017) Appl. Catal. B: Environ. 209:689–700

3. Zazhigalov S, Elyshev A, Lopatin S, Larina T, Cherepanova S, Mikenin P, Pisarev D, Baranov D, Zagoruiko A (2016) Reac. Kinet. Mech. Cat. 120:247–260
4. Suárez-Vázquez S, Gil S, García-Vargas J, Cruz-López A, Giroir-Fendler A (2018) Appl. Catal. B: Environ. 223:201–208
5. Chen J, Chen X, Chen X, Xu W, Xu Z, Jia H, Chen J (2018) Appl. Catal. B: Environ. 224:825–835
6. Giroir-Fendler A, Alves-Fortunato M, Richard M, Wang C, Díaz J, Gil S, Zhang C, Can F, Bion N, Guo Y (2016) Appl. Catal. B: Environ. 180:29–37
7. Chlala D, Giraudon J, Nuns N, Lancelot C, Vannier R, Labaki M, Lamonier J (2016) Appl. Catal. B: Environ. 184:87–95
8. Qu Z, Bu Y, Qin Y, Wang Y, Fu Q (2013) Appl. Catal. B: Environ. 132–133:353–362
9. Rokicińska A, Drozdek M, Dudek B, Gil B, Michorczyk P, Brouri D, Dzwigaj S, Kuśtrowski P (2017) Appl. Catal. B: Environ. 212:59–67
10. Ye Z, Giraudon J, Nuns N, Simon P, Geyter N, Morent R, Lamonier J (2018) Appl. Catal. B: Environ. 223:154–166
11. Wei Y, Ni L, Li M, Zhao J (2017) Catal Today 297:188–192
12. Wang C, Zhang C, Hua W, Guo Y, Lu G, Gil S, Giroir-Fendler A (2017) Chem Eng J 315:392–402
13. Wang X, Kang Q, Li D (2009) Appl. Catal. B: Environ. 86:166–175
14. Shi L, Chu W, Qu F, Hu J, Li M (2008) J Rare Earths 26:836
15. Wang Z, Shen G, Li J, Liu H, Wang Q, Chen Y (2013) Appl. Catal. B: Environ. 138–139:253–259
16. Venkataswamy P, Jampaiah D, Rao K, Reddy B (2014) Appl. Catal. A: Gen. 488:1–10
17. Li T, Chiang S, Liaw B, Chen Y (2011) Appl. Catal. B: Environ. 103:143–148
18. Hu F, Chen J, Peng Y, Song H, Li K, Li J (2018) Chem Eng J 331:425–434
19. Cheng Z, Chen Z, Li J, Zuo S, Yang P (2018) Appl Surf Sci 459:32–39
20. He C, Xu B, Shi J, Qiao N, Hao Z, Zhao J (2015) Fuel Process Technol 130:179–187
21. Du J, Qu Z, Dong C, Song L, Qin Y, Huang N (2018) Appl Surf Sci 433:1025–1035
22. Fang Z, Yuan B, Lin T, Xu H, Cao Y, Shi Z, Gong M, Chen Y (2015) Che. Eng. Res. Des. 94:648–659
23. Arena F, Trunfio G, Negro J, Spadaro L (2008) Mater Res Bull 43:539–545
24. Hussain S, Sayari A, Larachi F (2001) Appl. Catal. B: Environ. 34:1–9
25. Yang P, Yang S, Shi Z, Tao F, Guo X, Zhou R (2016) Chem Eng J 285:544–553
26. Zhang X, Hou F, Yang Y, Wang Y, Liu N, Chen D, Yang Y (2017) Appl Surf Sci 423:771–779
27. Liu P, Wei G, Liang X, Chen D, He H, Chen T, Xi Y, Chen H, Han D, Zhu J (2018) App. Clay Sci. 161:265–273
28. Kang M, Park E, Kim J, Yie J (2007) Appl. Catal. A: Gen. 327:261–269
29. Ahn C, You Y, Heo I, Hong J, Jeon J, Ko Y, Kim Y, Park H, Suh J (2017) J Ind Eng Chem 47:439–445
30. Yang P, Yang S, Shi Z, Meng Z, Zhou R (2015) Appl. Catal. B: Environ. 162:227–235
31. Ma L, Wang D, Li J, Bai B, Fu L, Li Y (2014) Appl. Catal. B: Environ. 148–149:36–43
32. Li L, Jing F, Yan J, Jing J, Chu W (2017) Catal Today 297:167–172
33. Laguna O, Romero Sarria F, Centeno M, Odriozola J (2010) J Catal 276:360–370
34. Liao Y, Fu M, Chen L, Wu J, Huang B, Ye D (2013) Catal Today 216:221–228
35. Venkataswamy P, Rao K, Jampaiah D, Reddy B (2015) Appl. Catal. B: Environ. 162:122–132
36. Fallah J, Hilaire L, Roméo M, Normand F (1995) J. Electron. Spectrosc. Rel. Phenom. 73:89–103
37. Hu Z, Qiu S, You Y, Guo Y, Guo Y, Wang L, Zhan W, Lu G (2018) Appl. Catal. B: Environ. 225:110–120
38. Torrente-Murciano L, Gilbank A, Puertolas B, Garcia T, Solsona B, Chadwick D (2013) Appl. Catal. B: Environ. 132–133:116–122
39. Delimaris D, Ioannides T (2008) Appl. Catal. B: Environ. 84:303–312
40. Tang X, Li Y, Huang X, Xu Y, Zhu H, Wang J, Shen W (2006) Appl. Catal. B: Environ. 62:265–273
41. Santos V, Pereira M, Órfão J, Figueiredo J (2010) Appl. Catal. B: Environ. 99:353–363
42. Yu D, Liu Y, Wu Z (2010) Catal Commun 11:788–791
43. Hu S, He L, Wang Y, Su S, Jiang L, Chen Q, Liu Q, Chi H, Xiang J, Sun L (2016) Int. J. Hydrog. Energy 41:17967–17975
44. Zhao X, Li H, Zhang J, Shi L, Zhang D (2016) Int. J. Hydrog. Energy 41:2447–7456
45. Hou Z, Feng J, Lin T, Zhang H, Zhou X, Chen Y (2018) Appl Surf Sci 434:82–90
46. Wang H, Guo W, Jiang Z, Yang R, Jiang Z, Pan Y, Shangguan W (2018) J Catal 361:370–383
47. Tan W, Deng J, Xie S, Yang H, Jiang Y, Guo G, Dai H (2015) Nanoscale 7:8510–8523

48. Rivas B, López-Fonseca R, Sampedro C, Gutiérrez-Ortiz J (2009) Appl. Catal. B: Environ. 90:545–555
49. Gutiérrez-Ortiz J, Rivas B, López-Fonseca R, González-Velasco J (2006) Appl. Catal. B: Environ. 65:191–200
50. Hu F, Chen J, Zhao S, Li K, Si W, Song H, Li J (2017) Appl. Catal. A: Gen. 540:57–67
51. Long G, Chen M, Li Y, Ding J, Sun R, Zhou Y, Huang X, Han G, Zhao W (2018) Chem Eng J. https://doi.org/10.1016/j.cej.2018.07.091
52. Deng L, Ding Y, Duan B, Chen Y, Li P, Zhu S, Shen S (2018) Mol. Catal. 446:72–80